

An adaptive transport framework for joint and conditional density estimation

Ricardo Baptista

Massachusetts Institute of Technology
Cambridge, MA, 02139, USA
rsb@mit.edu

Youssef Marzouk

Massachusetts Institute of Technology
Cambridge, MA, 02139, USA
ymarz@mit.edu

Olivier Zahm

Univ. Grenoble Alpes, Inria, CNRS, Grenoble INP, LJK
38000, Grenoble, France
olivier.zahm@inria.fr

Abstract

We propose a general framework to robustly characterize joint and conditional probability distributions via transport maps. Transport maps or “flows” deterministically couple two distributions via an expressive monotone transformation. Yet, learning the parameters of such transformations in high dimensions is challenging given few samples from the unknown target distribution, and structural choices for these transformations can have a significant impact on performance. Here we formulate a systematic framework for representing and learning monotone maps, via invertible transformations of smooth functions, and demonstrate that the associated minimization problem has a unique global optimum. Given a hierarchical basis for the appropriate function space, we propose a sample-efficient adaptive algorithm that estimates a sparse approximation for the map. We demonstrate how this framework can learn densities with stable generalization performance across a wide range of sample sizes on real-world datasets.

1 Introduction

The density π of a set of random variables $\mathbf{X} \in \mathbb{R}^d$ is a core object in statistics and machine learning. Many inference, prediction, and sampling algorithms rely on evaluations of π , or of certain conditionals of π ; yet in practice, we may only have access to a small sample of independent observations $\{\mathbf{x}^i\}$ from π . This paper addresses the fundamental task of robustly estimating the joint density and its conditionals from data.

One popular approach for density estimation is to couple π with a tractable reference density η . Given two probability measures ν_π and ν_η on \mathbb{R}^d , assumed to have densities π and η respectively, a *coupling* is a pair of random variables \mathbf{X} and \mathbf{Z} which admit π and η as marginals. One special kind of coupling is given by a deterministic transformation $S: \mathbb{R}^d \rightarrow \mathbb{R}^d$ such that $S(\mathbf{X}) = \mathbf{Z}$ in distribution. The transformation S that satisfies this property is called a *transport map* [39].

In this work we characterize the density π by learning a monotone triangular map S . Triangular maps define an autoregressive model where each component represents one marginal conditional in the factorization of π . In recent years, several parameterizations have been proposed for triangular maps. These include maps based on polynomials [21, 15], radial basis functions [36], and neural networks of varying capacity [9, 16]. Furthermore, these maps have been composed to define complex transformations known as normalizing flows [18, 27]. These flows were successfully used in several

applications including density estimation [28]; variational inference [30, 5]; generation of images, video, and other structured objects [25, 16]; and likelihood-free inference [26].

Despite the empirical success of different parameterizations, little work has addressed the properties of the optimization problems for triangular transport maps. Our contributions are as follows. We present a systematic framework for representing and learning monotone triangular maps. Our approach relies on an operator that transforms broad classes of smooth functions into monotone functions. From the theoretical perspective, we show that the associated optimization problem is *well-defined* and *continuous* under appropriate tail conditions; we also demonstrate that it has a unique global minimum. Algorithmically, we then describe an adaptive procedure for selecting appropriate smooth functions given a hierarchical basis of the corresponding function space. The procedure naturally produces map representations that are *parsimonious* and *interpretable*—in particular, it exploits and implicitly discovers conditional independence structure. Maintaining a strict triangular map also exposes all marginal conditionals of the joint density, immediately enabling *conditional density estimation*. Our numerical experiments show that the algorithm provides robust performance at small-to-moderate sample sizes, and constitutes a semiparametric approach that naturally links map complexity to the size of the data.

Proofs, additional results, and details pertaining to the numerical experiments are available in the Supplementary Material. The corresponding sections are referenced within the article as SM.#

2 Transport maps for density estimation

We consider the unsupervised learning problem of approximating a target probability density function $\pi(\mathbf{x})$ defined on \mathbb{R}^d using i.i.d. samples from π . Our objective is to construct a differentiable transport map $S: \mathbb{R}^d \rightarrow \mathbb{R}^d$ such that the pullback density

$$S^\# \eta(\mathbf{x}) = \eta \circ S(\mathbf{x}) \det \nabla S(\mathbf{x}), \quad (1)$$

is an approximation to π . Here, we choose η to be the probability density function of the standard normal distribution on \mathbb{R}^d . With this choice, S *pushes forward* the random vector $\mathbf{X} \sim \pi$ into a standard normal vector $S(\mathbf{X}) \sim \eta$. For an invertible S , we can generate samples from π by generating samples $\mathbf{z} \sim \eta$ and evaluating $S^{-1}(\mathbf{z})$.

We consider an increasing lower triangular map $S(\mathbf{x}): \mathbb{R}^d \rightarrow \mathbb{R}^d$, meaning a map of the form

$$S(\mathbf{x}) = \begin{bmatrix} S^1(x_1) \\ S^2(x_1, x_2) \\ \vdots \\ S^d(x_1, \dots, x_d) \end{bmatrix}, \quad (2)$$

where each of the d components $S^k: \mathbb{R}^k \rightarrow \mathbb{R}$ is a continuously differentiable function such that $x_k \mapsto S^k(\mathbf{x}_{<k}, x_k)$ is strictly monotone increasing for all $\mathbf{x}_{<k} = (x_1, \dots, x_{k-1}) \in \mathbb{R}^{k-1}$. Such a map has the advantage of being easy to invert¹ and has a lower triangular Jacobian $\nabla S(\mathbf{x})$ so that $\det \nabla S(\mathbf{x}) = \prod_{i=1}^d \partial_{x_i} S^i(\mathbf{x}_{1:i})$ is readily computable.

Under natural assumptions on π and η ,² the *Knothe–Rosenblatt* (KR) rearrangement S_{KR} is the unique increasing lower triangular map as in (2) such that $\pi(\mathbf{x}) = S_{\text{KR}}^\# \eta(\mathbf{x})$; see [31, 17, 4, 39]. We propose to approximate S_{KR} by minimizing the Kullback–Leibler (KL) divergence from $S^\# \eta$ to π , $\mathcal{D}_{\text{KL}}(\pi \| S^\# \eta) = \mathbb{E}_\pi [\log(\pi(\mathbf{x})/S^\# \eta(\mathbf{x}))]$. With the standard normal reference $\eta(\mathbf{z}) = (2\pi)^{-d/2} \exp(-\|\mathbf{z}\|^2/2)$ we can decompose the KL divergence as

$$\mathcal{D}_{\text{KL}}(\pi \| S^\# \eta) = \mathbb{E}_\pi [\log \pi(\mathbf{x})] + \frac{d}{2} \log(2\pi) + \sum_{k=1}^d \mathcal{J}_k(S^k), \quad (3)$$

where the objective functions $\mathcal{J}_1, \dots, \mathcal{J}_d$ are given by

$$\mathcal{J}_k(s) := \mathbb{E}_\pi \left[\frac{1}{2} s(\mathbf{X}_{1:k})^2 - \log |\partial_k s(\mathbf{X}_{1:k})| \right]. \quad (4)$$

¹For any $\mathbf{z} \in \mathbb{R}^d$, $\mathbf{x} = S^{-1}(\mathbf{z})$ can be computed recursively by $x_k = T^k(\mathbf{x}_{1:k-1}, z_k)$ for $k = 1, \dots, d$, where $T^k(\mathbf{x}_{1:k-1}, \cdot)$ is the inverse function of $x_k \mapsto S^k(\mathbf{x}_{1:k-1}, x_k)$.

²It is sufficient for π and η to be strictly positive densities on \mathbb{R}^d .

Each \mathcal{J}_k is a strictly convex function, see SM.1. Thus, minimizing $s \mapsto \mathcal{J}_k(s)$ over functions $s: \mathbb{R}^k \rightarrow \mathbb{R}$ such that $\partial_k s(\mathbf{x}_{1:k}) > 0$ is a strictly convex problem. Furthermore, the decomposition (3) into d objective functions allows the components S^k to be computed independently in parallel.

Given n independent samples $\{\mathbf{x}^i\}_{i=1}^n \sim \pi$, we replace the expectation in (4) by a sample average

$$\hat{\mathcal{J}}_k(s) := \frac{1}{n} \sum_{i=1}^n \left[\frac{1}{2} s(\mathbf{x}_{1:k}^i)^2 - \log |\partial_k s(\mathbf{x}_{1:k}^i)| \right]. \quad (5)$$

Minimizing (5) under the constraint $\partial_k s(\mathbf{x}_{1:k}) > 0$ remains a convex problem. The solution yields an estimator \hat{S}^k for S_{KR}^k , and the collection of all components defines an estimator for the KR rearrangement \hat{S} that approximates the joint density $\pi(\mathbf{x})$ as $\hat{\pi}(\mathbf{x}) = \hat{S}^\# \eta(\mathbf{x})$.

Conditional density estimation. We also consider the supervised learning problem of approximating the conditional probability density function $\pi(\mathbf{x}|\mathbf{y})$ using i.i.d. samples $\{(\mathbf{x}^i, \mathbf{y}^i)\}_{i=1}^n$ from the joint density $\pi(\mathbf{x}, \mathbf{y})$. Here, $\mathbf{x} \in \mathbb{R}^d$ and $\mathbf{y} \in \mathbb{R}^m$. For this task, we use an increasing lower triangular map $S: \mathbb{R}^{m+d} \rightarrow \mathbb{R}^{m+d}$ with the following structure

$$S(\mathbf{y}, \mathbf{x}) = \begin{bmatrix} S^{\mathcal{Y}}(\mathbf{y}) \\ S^{\mathcal{X}}(\mathbf{y}, \mathbf{x}) \end{bmatrix}, \quad (6)$$

where $S^{\mathcal{Y}}(\cdot): \mathbb{R}^m \rightarrow \mathbb{R}^m$ and $S^{\mathcal{X}}(\mathbf{y}, \cdot): \mathbb{R}^d \rightarrow \mathbb{R}^d$ are increasing lower triangular maps for any $\mathbf{y} \in \mathbb{R}^m$. Recall that the reference density $\eta(\mathbf{x}, \mathbf{y})$ is standard normal, and thus factorizes as $\eta(\mathbf{x}, \mathbf{y}) = \eta_1(\mathbf{y})\eta_2(\mathbf{x})$. The corresponding KR rearrangement $S_{\text{KR}}(\mathbf{y}, \mathbf{x})$ as in (6) allows writing the marginal density of \mathbf{y} as $\pi(\mathbf{y}) = (S_{\text{KR}}^{\mathcal{Y}})^\# \eta_1(\mathbf{y})$ and, more interestingly, it exposes the conditional density of \mathbf{x} given \mathbf{y} as $\pi(\mathbf{x}|\mathbf{y}) = (S_{\text{KR}}^{\mathcal{X}}(\mathbf{y}, \cdot))^\# \eta_2(\mathbf{x})$.

The last d components of the KR rearrangement, $S_{\text{KR}}^{\mathcal{X},k}(\mathbf{y}, \mathbf{x}_{1:k})$, $1 \leq k \leq d$, can be estimated from independent samples $\{\mathbf{x}^i, \mathbf{y}^i\}_{i=1}^n \sim \pi(\mathbf{x}, \mathbf{y})$ by minimizing the sample averages

$$\hat{\mathcal{J}}_k^{\mathcal{X}}(s) := \frac{1}{n} \sum_{i=1}^n \left[\frac{1}{2} s(\mathbf{y}^i, \mathbf{x}_{1:k}^i)^2 - \log |\partial_{m+k} s(\mathbf{y}^i, \mathbf{x}_{1:k}^i)| \right], \quad (7)$$

under the constraints $\partial_{m+k} s(\mathbf{y}, \mathbf{x}_{1:k}) > 0$. This produces an estimator $\hat{S}^{\mathcal{X}}$ of $S_{\text{KR}}^{\mathcal{X}}$ which in turn approximates the conditional density $\pi(\mathbf{x}|\mathbf{y})$ as $\hat{\pi}(\mathbf{x}|\mathbf{y}) := (\hat{S}^{\mathcal{X}}(\mathbf{y}, \cdot))^\# \eta_2(\mathbf{x})$.

3 Monotone transport maps

In this section we propose a general representation for each transport map component S^k which enforces the monotonicity constraint $\partial_k S^k(\mathbf{x}_{1:k}) > 0$ by construction. For any sufficiently smooth $f: \mathbb{R}^k \rightarrow \mathbb{R}$ we let $\mathcal{R}_k(f): \mathbb{R}^k \rightarrow \mathbb{R}$ be the function defined by

$$\mathcal{R}_k(f)(\mathbf{x}_{1:k}) := f(\mathbf{x}_{<k}, 0) + \int_0^{\mathbf{x}_k} g(\partial_k f(\mathbf{x}_{<k}, t)) dt, \quad (8)$$

where $g: \mathbb{R} \rightarrow \mathbb{R}_{>0}$ is a positive function. We call the operator $\mathcal{R}_k: f \mapsto \mathcal{R}_k(f)$ a *rectifier* because it transforms any f into a function that is increasing in the k -th variable, i.e., $\partial_k \mathcal{R}_k(f)(\mathbf{x}_{1:k}) = g(\partial_k f(\mathbf{x}_{1:k})) > 0$. For instance, the zero function $f(\mathbf{x}_{1:k}) = 0$ is rectified into the linear function $\mathcal{R}_k(f)(\mathbf{x}_{1:k}) = g(0)x_k$. With the parametrization $s = \mathcal{R}_k(f)$, the constrained minimization problem $\min_{\{s: \partial_k s > 0\}} \mathcal{J}_k(s)$ becomes the unconstrained problem $\min_f \mathcal{L}_k(f)$ where

$$\mathcal{L}_k(f) := \mathcal{J}_k(\mathcal{R}_k(f)).$$

By introducing the rectifier, we lose the convexity of the original problem but we obtain an unconstrained minimization problem.

The choice of the function g in (8) is essential. A popular choice is the square function $g(\xi) = \xi^2$ [15, 5]. This is convenient because it permits the integral in (8) to be computed in closed form when f is polynomial. Instead, here we consider the modified soft-plus function

$$g(\xi) := \log(2^\xi + 1) / \log(2), \quad (9)$$

which satisfies $g(0) = 1$ (so that $f(\mathbf{x}_{1:k}) = 0$ is rectified into $\mathcal{R}_k(f)(\mathbf{x}_{1:k}) = x_k$). In contrast to the square function, this g is invertible with $g^{-1}(\xi) = \log(2^\xi - 1)/\log(2)$. As a consequence, \mathcal{R}_k is also invertible, and for any sufficiently smooth $s: \mathbb{R}^k \rightarrow \mathbb{R}$ with $\partial_k s(\mathbf{x}_{1:k}) > 0$, we have

$$\mathcal{R}_k^{-1}(s)(\mathbf{x}_{1:k}) := s(\mathbf{x}_{<k}, 0) + \int_0^{x_k} g^{-1}(\partial_k s(\mathbf{x}_{<k}, t)) dt. \quad (10)$$

More importantly, the choice (9) for g yields an objective function \mathcal{L}_k that is far better behaved in terms of the optimization procedure for f ; see the numerical illustration in Figure 1. We observe that $\mathcal{L}_k = \mathcal{J}_k \circ \mathcal{R}_k$, though non-convex, has no local minima or saddle points. The following proposition provides intuition for this observation: composition with a smooth invertible map preserves the global minima of a smooth convex function.³ The proof is provided in SM.1.

Proposition 1. *Let $j: \mathbb{R}^m \rightarrow \mathbb{R}$ be a convex C^1 function and let $r: \mathbb{R}^m \rightarrow \mathbb{R}^m$ be a C^1 -diffeomorphism. Then any critical point of $j \circ r$ is a global minimum of $j \circ r$. Furthermore if j is strictly convex, then the global minimum of $j \circ r$ is unique.*

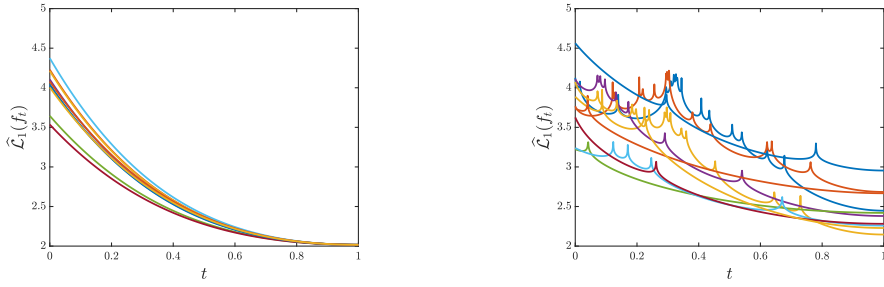


Figure 1: Objective function $\hat{\mathcal{L}}_1 = \hat{\mathcal{J}}_1 \circ \mathcal{R}_1$ using either the modified soft-plus function g (9) (left) or the square function $g(\xi) = \xi^2$ (right). Here, $\pi(x) = \mathcal{N}(x; -2, 0.5) + \mathcal{N}(x; 2, 2)$ is a one-dimensional Gaussian mixture and we use $n = 50$ to estimate \mathcal{J}_1 . The objective is evaluated along line segments that interpolate between random initial maps ($t = 0$) and critical points resulting from a gradient-based optimization method ($t = 1$). Observe also that with the modified soft-plus function g (left) the algorithm always arrives at the same optimal value (at $t = 1$), whereas with the square function g (right) the algorithm gets stuck in local minima and rarely attains the optimal value.

Now, to develop a function-analytic framework for constructing f , we let

$$H^{1,k}(\mathbb{R}^k) := \left\{ f: \mathbb{R}^k \rightarrow \mathbb{R} \text{ such that } \int |f(\mathbf{x})|^2 + |\partial_k f(\mathbf{x})|^2 d\mathbf{x} < +\infty \right\} \quad (11)$$

be the Hilbert space of functions endowed with the norm $\|\cdot\|_{H^{1,k}}$ such that $\|f\|_{H^{1,k}}^2 := \|f\|_{L^2}^2 + \|\partial_k f\|_{L^2}^2$ for all $f \in H^{1,k}(\mathbb{R}^k)$. Intuitively, $H^{1,k}(\mathbb{R}^k)$ is the subset of $L^2(\mathbb{R}^k) := \{f: \mathbb{R}^k \rightarrow \mathbb{R}, \int |f(\mathbf{x})|^2 d\mathbf{x} < +\infty\}$ that contains all antiderivatives (in the k -th variable) of functions in $L^2(\mathbb{R}^k)$. The following proposition shows that the objective function \mathcal{L}_k , seen as a function from $H^{1,k}(\mathbb{R}^k)$ to \mathbb{R} , is well-defined and continuous.

Proposition 2. *Assume there exists a constant $C_\pi < \infty$ such that $\pi(\mathbf{x}) \leq C_\pi \eta(\mathbf{x})$ for any $\mathbf{x} \in \mathbb{R}^d$, and choose g to be the soft-plus function (9). Then $\mathcal{L}_k(f) < \infty$ for any $f \in H^{1,k}(\mathbb{R}^k)$. Moreover, $\mathcal{L}_k: H^{1,k}(\mathbb{R}^k) \rightarrow \mathbb{R}$ is a continuous function.*

It is useful to discuss certain implications of seeking f in $H^{1,k}(\mathbb{R}^k)$. To exactly recover the KR rearrangement S_{KR} by minimizing \mathcal{L}_k over $H^{1,k}(\mathbb{R}^k)$, it is necessary that $\mathcal{R}_k^{-1}(S_{\text{KR}}^k) \in H^{1,k}(\mathbb{R}^k)$ for all $1 \leq k \leq d$. If this is true, then $\partial_k \mathcal{R}_k^{-1}(S_{\text{KR}}^k)$ is square integrable, and so $\partial_k \mathcal{R}_k^{-1}(S_{\text{KR}}^k)(\mathbf{x}_{1:k}) = g^{-1}(\partial_k S_{\text{KR}}^k(\mathbf{x}_{1:k}))$ must go to zero when $\|\mathbf{x}\| \rightarrow \infty$. By continuity of g we have

$$\partial_k S_{\text{KR}}^k(\mathbf{x}_{1:k}) \xrightarrow{\|\mathbf{x}\| \rightarrow \infty} g(0) = 1,$$

³Formalizing this proposition for \mathcal{L}_k requires analyzing the higher-order smoothness properties of the operator \mathcal{R}_k , which we leave to future work.

which means that the KR rearrangement behaves as the identity map when $\|x\| \rightarrow \infty$. This implies that the tails of $\pi = S_{\text{KR}}^\# \eta$ are the same as the tails of η —i.e., Gaussian, which is consistent with the condition imposed on the target density in Proposition 2. Conversely, if the density π does not have Gaussian tails, then it is not possible to exactly recover the KR rearrangement by seeking f in $H^{1,k}(\mathbb{R}^k)$. However, this does not imply that we cannot obtain good estimates $\hat{S}^\# \eta$ for π given finite samples; rather, it affects the asymptotic ($n \rightarrow \infty$) bias of the estimator in this setting.

Related work. Many normalizing flow architectures also enforce monotonicity of the map components by making structural choices for S^k [28, 14, 11]. Recently, [41] considered the rectifier in (8) to represent S^k using a shifted exponential linear unit function g and unconstrained neural networks for f . With this choice of g , \mathcal{R}_k is invertible and \mathcal{L}_k again should not have local minima or saddle points with respect to f . However, there is no evidence that the function \mathcal{L}_k has favorable optimization properties over the considered function space of neural networks, and the associated nonlinear parameterization of f certainly introduces critical points that are not global minima.

An alternative to monotone parameterizations is to enforce the monotonicity constraint for S^k at a finite collection of samples x^i . For instance, in [29] the authors satisfy this constraint at the samples used to approximate the objective function in (5). This approach results in a convex optimization problem under a linear expansion for S^k . However, in a setting with few samples, this relaxation of the constraint may not be sufficient to guarantee monotonicity of S^k over the full support of π .

4 Adaptive transport map algorithm

We now propose an adaptive algorithm to learn the function $f \in H^{1,k}(\mathbb{R}^k)$ that minimizes the objective $\hat{\mathcal{L}}_k$. We consider linear expansions $f(x_{1:k}) = \sum_{\alpha} c_{\alpha} \psi_{\alpha}(x_{1:k})$, where $c_{\alpha} \in \mathbb{R}$ are parameters and $\psi_{\alpha}: \mathbb{R}^k \rightarrow \mathbb{R}$ are features specified by a multi-index $\alpha = (\alpha_1, \dots, \alpha_k) \in \mathbb{N}_0^k$. We construct these features as products of univariate features, i.e., $\psi_{\alpha}(x_{1:k}) = \prod_{j=1}^k \psi_{\alpha_j}(x_j)$. Given a set of features, we solve the unconstrained minimization problem over the collection of parameters (c_{α}) to learn f . We note that linear expansions for f transfer the good properties of the objective \mathcal{L}_k (as in Figure 1) to the objective function over the coefficients (c_{α}).

In a setting with few samples from π , we seek a sparse representation of f that balances the bias with the variance of the approximation. In general, the success of this representation depends on whether the true map can be sparsely represented using the selected features. For example, in numerical analysis, orthogonal polynomials have long been shown to be effective features for the sparse approximation of smooth solutions to high-dimensional parameterized PDEs [10, 8, 7]. Here we employ univariate features given by Hermite functions $\psi_{\alpha_j}(x) = P_{\alpha_j}(x) \exp(-x^2/4)$, where P_{α_j} are orthonormal Hermite polynomials with respect to the density $\eta(x)$ ⁴. For numerical stability in high-dimensions, we also append constant univariate functions to the considered set of features. We emphasize, however, that our framework can generally be applied with *any* set of features in $H^{1,k}(\mathbb{R}^k)$. To this end, a basis of smooth wavelets [13] is another attractive choice, which we will explore in future work.

Finding a sparse approximation given a (possibly infinite) set of features is in general a combinatorial problem. To make this problem tractable, we consider a greedy enrichment procedure that does not require prescribing a full collection of features in advance. This procedure maintains an *active set* of multi-indices Λ_t corresponding to the features in the current expansion, f_t , at iteration t . In each iteration, the algorithm adds one multi-index to Λ_t that reduces the value of the objective function. We begin with $\Lambda_0 = \emptyset$, which corresponds to $f_0 = 0$ and the identity map $\mathcal{R}_k(f_0)(x_{1:k}) = x_k$.

In general, finding a multi-index in \mathbb{N}_0^k to add to Λ_t that is not in the active set requires testing an infinite number of candidate features at each iteration. For tractability, we restrict Λ_t to be a downward-closed multi-index set (i.e., if $\alpha \in \Lambda_t$ and $\alpha' \leq \alpha$, then $\alpha' \in \Lambda_t$) and reduce the search-space to multi-indices in the *reduced margin* of Λ_t as in [6]. The reduced margin is defined as the set Λ_t^{RM} such that the union of any multi-index $\alpha \in \Lambda_t^{\text{RM}}$ and the active set remains downward closed. The reduced margin is a subset of the margin set Λ_t^{M} (i.e., multi-indices $\alpha \notin \Lambda_t$ such that $\exists l > 0$ where $\alpha - \mathbf{e}_l \in \Lambda_t$); see Figure 2. Thus, searching in the reduced margin typically requires

⁴Hence, these Hermite functions $\psi_{\alpha_j} \in H^{1,k}(\mathbb{R})$ form an orthogonal basis for $L^2(\mathbb{R})$.

testing fewer features. The reduced margin also grows more *slowly* with respect to the dimension k than the margin. For instance, if Λ_t contains all multi-indices in a hypercube of width p in dimension k , the margin has cardinality $(p+1)^k - p^k$, while the reduced margin has cardinality k .

In each iteration, we evaluate the gradient of the objective function with respect to the features in the reduced margin and use a heuristic to choose a new multi-index $\alpha_t^* \in \arg \max_{\alpha \in \Lambda_t^{\text{RM}}} |\nabla_{c_\alpha} \hat{\mathcal{L}}_k(f^k)|$. We add α_t^* to the active set and update our approximation to f by optimizing all of the parameters for the features in the active set. We repeat these steps for m iterations (i.e., adding m features in total).

Remark 1. *Optimizing all of the parameters in each iteration is analogous to the projection step in orthogonal matching pursuit for sparse regression [37]. A less expensive variant of the algorithm only optimizes the parameter for each new feature, as in matching pursuit. A comparison of the trade-offs between these algorithms for density estimation is an interesting direction of future work.*

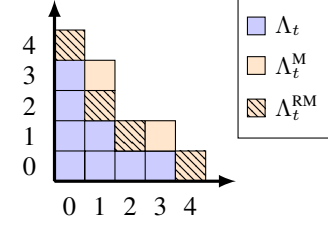


Figure 2: A $k = 2$ dimensional downward-closed active set of multi-indices Λ_t with its margin Λ_t^M and reduced margin Λ_t^{RM}

The algorithm for learning each map component is presented in detail in SM.2. To select the total number of features m , we use K -fold cross-validation. We repeat the algorithm with K different training sets and select m (i.e., the number of iterations) that minimizes the average of the objective functions $\hat{\mathcal{L}}_k$ evaluated using independent validation sets. In our experiments we consider $m \in [1, \sqrt{n}]$ as in [40]. We call this complete procedure the Adaptive Transport Map (ATM) algorithm.

5 Numerical experiments

In this section, we evaluate the performance of the ATM algorithm on several joint and conditional density estimation problems. §5.1 illustrates benefits of adaptivity; §5.2–5.4 demonstrate how the estimated maps reveal and exploit structure in the target density; and §5.5 presents conditional density estimation results on a suite of UCI datasets. Additional experiments to visualize the expressiveness of the selected features for representing the map are reported in SM.3.

In all of the numerical experiments, we pre-process the data by subtracting the empirical mean and dividing each variable by its empirical standard deviation. We evaluate the monotone map in (8) by performing numerical integration using an adaptive quadrature method with a relative error of 10^{-3} . At each iteration of the ATM algorithm, we optimize the parameters c_α for $\alpha \in \Lambda_t$ using a BFGS quasi-Newton method [24]. To assess the quality of $\hat{\pi}$ given a training set, we evaluate the negative log-likelihood of the approximate (joint or conditional) density on a common test set. The negative log-likelihood is an estimator for $-\mathbb{E}_\pi[\log \hat{S}^\# \eta] = \frac{d}{2} \log(2\pi) + \sum_{k=1}^d \mathcal{J}_k(\hat{S}^k)$. We note that this is an offset of the KL divergence and thus lower is better. The mean negative log-likelihood and a 95% confidence interval for the mean are reported over different training sets.

5.1 Mixture of Gaussians

We consider a 3-dimensional distribution defined as a mixture of Gaussians centered at the 8 vertices of the hypercube $[-4, 4]^3$, each with covariance matrix I_d . The weights of the mixture components were randomly sampled from a uniform distribution and normalized. Figure 3a plots the one and two-dimensional marginals of the joint density π . To estimate π , we generate $n = 100$ training samples $\{\mathbf{x}^i\}_{i=1}^n \sim \pi$ and use the ATM algorithm to estimate the KR rearrangement that pushes forward π to η . Figure 3b plots the marginals of $\hat{\pi}$. Figure 3c plots the mean negative log-likelihood of $\hat{\pi}$ on a test set of 10^5 samples for increasing sizes of the training set n . The performance of ATM is compared to a non-adaptive method that approximates each map component with a total-degree p expansion, i.e., a linear expansion in k variables with all features in $\Lambda = \{\alpha \in \mathbb{N}_0^k, \|\alpha\|_1 \leq p\}$. For each sample size n , ATM consistently finds a better estimator of π by identifying the necessary features to represent the map components.

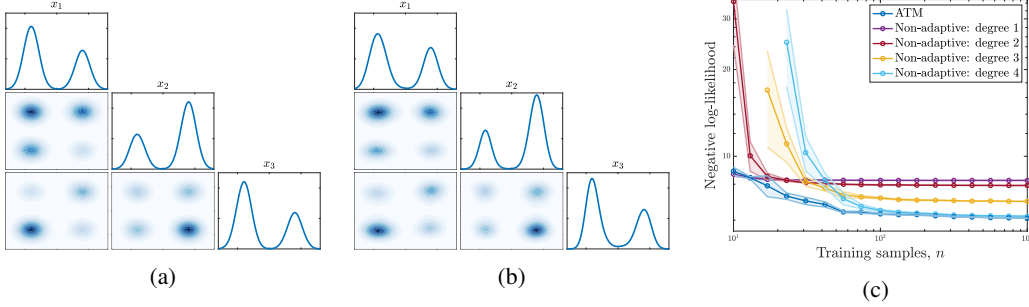


Figure 3: (a) The true density π . (b) An approximate density $\hat{\pi}$ using $n = 100$ samples. (c) The mean negative log-likelihood over 10 sets of training samples is lower for ATM than non-adaptive methods.

5.2 Gene dataset

Next we consider a $d = 39$ dimensional dataset that contains $n = 118$ samples for the expression levels of isoprenoid genes from the plant *Arabidopsis thaliana*.⁵ Algorithms for learning graphical models have used this non-Gaussian dataset to identify sparse dependencies between the genes [19].

A key property of triangular transport maps is that they inherit sparsity from the conditional independence structure of π . [35] showed that for η with independent components, the Markov structure associated with π yields a lower bound on the sparsity of the map S (i.e., the functional dependence of each component S^k on the input variables $x_{1:k-1}$). Thus, we expect the true KR rearrangement for this distribution to be sparse [22].

We follow the procedure in SM.4 to pre-process the dataset. Table 1 compares the mean negative log-likelihood from the ATM algorithm to density estimation methods based on high-capacity normalizing flows. These flows include variants of Masked Autoregressive Density Estimation (MADE) [12], Masked Autoregressive Flows (MAF) [28], and Neural Autoregressive Flows (NAF) [14]. We tuned the architecture and hyperparameters of each of these flows to achieve optimal performance, as detailed in SM.5. In comparison to many normalizing flows, the ATM algorithm takes advantage of the conditional independence structure in π to yield an estimator for $\hat{\pi}$ using a sparse map.

To account for linear correlations in the density, we also propose an algorithm that first applies ATM with linear features to learn a linear map \hat{S} , and then applies ATM with the Hermite function features using the pushforward of the training samples through the linear map. We denote this two-step algorithm as Linear+ATM in the table below. Linear+ATM has improved performance to the normalizing flows and requires significantly fewer parameters on average: 258 in Linear+ATM vs. 2.90×10^6 in NAF.

Table 1: Mean negative log-likelihood for the gene dataset over 20 sets of training samples

MADE	MADE-MoG	MAF	MAF-MADE	NAF	ATM	Linear+ATM
32.2 ± 3.7	31.8 ± 2.9	31.9 ± 3.3	29.8 ± 2.2	27.4 ± 4.8	31.7 ± 2.7	27.3 ± 2.8

5.3 Lorenz-96 dataset

Next we consider the $d = 20$ dimensional distribution of the state of the chaotic Lorenz-96 dynamical system at a fixed time. This system is a model for atmospheric quantities (e.g., temperature and vorticity) in mid-latitude regions of the Earth, and thus a popular testbed for data assimilation algorithms in numerical weather prediction (NWP) [34], where density estimation is an essential step.

To replicate the settings of large-scale NWP, we consider a small sample size $n = 100$ relative to the state dimension d . We generate training data using the procedure in SM.4. Table 2 compares the negative log-likelihood of the ATM algorithm on a common test set of 10^5 samples to the normalizing flow architectures considered in §5.2. ATM yields the best performance, without any manual hyperparameter optimization. Furthermore, Figure 4a shows how ATM is a semiparametric approach that

⁵A subset of 40 genes were considered in [43], but only 39 genes are available in the public dataset.

systematically increases the number of parameters describing the map as the number of training samples n rises, and consequently improves the negative log-likelihood of the approximation to π .

Table 2: Mean negative log-likelihood for the Lorenz-96 dataset over 5 sets of training samples

MADE	MADE-MoG	MAF	MAF-MADE	NAF	ATM
54.8 ± 0.7	55.6 ± 0.4	54.7 ± 0.2	57.2 ± 1.2	54.5 ± 0.3	54.0 ± 0.1

An additional feature of the ATM algorithm is the implicit discovery of conditional independence structure. Figure 4b plots the sparse variable dependence of the transport map \hat{S} found by ATM using $n = 316$ training samples; a non-filled entry (j, k) indicates that the k th map component does not depend on variable x_j . The banded variable dependence of the triangular map shows that each component of S depends strongly on neighboring variables in the physical grid. This closely matches the approximate conditional independence structure for the states of this dynamical system.

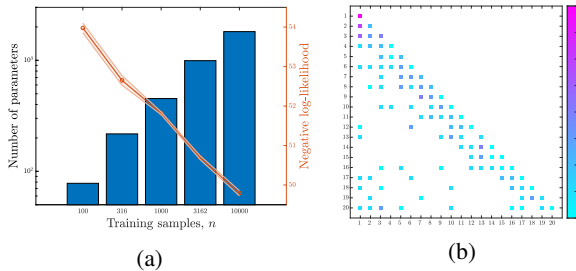


Figure 4: (a) The number of parameters vs. log-likelihood for the Lorenz-96 dataset with increasing sample size n . (b) The maximum multi-index of the features identified for each variable (*columns*) in each map component (*rows*).

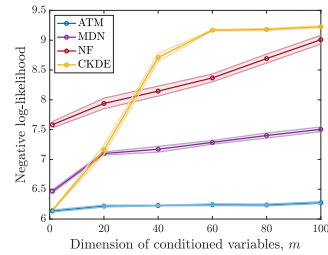


Figure 5: The negative log-likelihood of the conditional density from ATM is constant vs. the dimension of the uninformative covariates \mathbf{y} .

5.4 Conditional density estimation with uninformative covariates

Now we estimate the conditional density $\pi(\mathbf{x}|\mathbf{y})$ where $\mathbf{y} \in \mathbb{R}^m$ contains an increasing number of independent standard normal covariates and \mathbf{x} follows the distribution in §5.1. From the independence of \mathbf{x} and \mathbf{y} , we expect $\pi(\mathbf{x}|\mathbf{y}) = \pi(\mathbf{x})$ and the map block $S^{\mathcal{X}}(\mathbf{y}, \mathbf{x})$ in (6) to be only a function of \mathbf{x} .

Figure 5 plots the mean negative log-likelihoods of the approximate densities found with ATM over 5 sets of $n = 1000$ samples, compared to alternative high-capacity parametric and nonparametric methods for conditional density estimation. These include mixture density networks (MDN) [3], conditional normalizing flows (NF) [38], and conditional kernel density estimation (CKDE) [33]; implementation details are in SM.5. Compared to these methods, which do not exploit the conditional independence structure of π , ATM learns sparse maps that do not depend on the conditionally independent covariates \mathbf{y} , and thus achieves a negative log-likelihood independent of m .

5.5 Conditional density estimation on UCI datasets

Lastly, we evaluate ATM’s performance for conditional density estimation on a suite of UCI datasets. These datasets have one-dimensional variables x (i.e., $d = 1$) and require estimating one map component $S^{\mathcal{X}}(\mathbf{y}, x)$ for \mathbf{y} of varying dimension. We follow SM.4 to pre-process each dataset. For this example, we add an ℓ_2 regularization term for the map coefficients with a penalty of 10^{-4} .

Table 3 presents the mean negative log-likelihoods over 10 splits of the training data. To the best of our knowledge, many normalizing flow architectures do not currently support conditional density estimation. Hence, we compare ATM with up to $m = 100$ features to the methods presented in §5.4 as well as to ϵ -neighborhood kernel density estimation (NKDE) and kernel mixture networks (KMN) [2] using the implementation provided by [32]. For all datasets, we observe comparable performance of ATM to neural-network based methods and improved performance with our semiparametric method in comparison to non-parametric approaches (e.g., on the Concrete and Yacht datasets).

Table 3: Mean negative log-likelihood for UCI datasets over 10 sets of training samples. The method with best performance from both categories is highlighted in bold.

Dataset	ATM	CKDE	NKDE	MDN	KMN	NF
Boston	2.69 \pm 0.09	2.62 \pm 0.10	3.20 \pm 0.14	2.41 \pm 0.07	2.55 \pm 0.08	2.47 \pm 0.05
Concrete	3.08 \pm 0.05	3.23 \pm 0.03	3.91 \pm 0.05	2.85 \pm 0.04	3.16 \pm 0.03	3.19 \pm 0.06
Energy	1.32 \pm 0.03	0.97 \pm 0.05	2.04 \pm 0.03	1.20 \pm 0.03	1.68 \pm 0.05	1.70 \pm 0.13
Yacht	0.57 \pm 0.10	1.13 \pm 0.12	3.81 \pm 0.08	0.71 \pm 0.10	1.73 \pm 0.12	1.25 \pm 0.15

6 Conclusion

This paper presents a systematic framework for representing and estimating triangular transport maps for joint and conditional density estimation. It combines a well-behaved optimization problem with an adaptive semiparametric procedure to learn parsimonious maps with interpretable structure. An important future research direction is to integrate an approximation theoretic analysis of these maps with finite-sample estimation guarantees, for a broad class of distributions, particularly for applications with limited data such as likelihood-free Bayesian inference and structure learning.

Broader Impact

This work provides a principled approach for representing and approximating probability densities, with favorable theoretical and algorithmic properties. These properties are crucial for the automatic deployment of density estimation and inference algorithms in large-scale societal applications, such as numerical weather prediction and infectious disease modeling. For these problems, it is crucial that algorithms be flexible at capturing complex structure in data, but also robust in settings with limited observations. Our framework provides a rigorous and systematic approach for building models that are stable across a range of data sizes, which is important when making decisions based on probabilities and scenarios derived from these models.

Acknowledgments

RB, OZ, and YM gratefully acknowledge support from the INRIA associate team Unquestionable. RB and YM are also grateful for the support from the AFOSR Computational Mathematics program (MURI award FA9550-15-1-0038) and the US Department of Energy AEOLUS project. RB also acknowledges support from a NSERC PGSD-D fellowship.

References

- [1] Robert A Adams and John JF Fournier. *Sobolev spaces*. Elsevier, 2003.
- [2] Luca Ambrogioni, Umut Güçlü, Marcel AJ van Gerven, and Eric Maris. The kernel mixture network: A nonparametric method for conditional density estimation of continuous random variables. *arXiv preprint arXiv:1705.07111*, 2017.
- [3] Christopher M Bishop. Mixture density networks. Technical report, Aston University, 1994.
- [4] Vladimir Igorevich Bogachev, Aleksandr Viktorovich Kolesnikov, and Kirill Vladimirovich Medvedev. Triangular transformations of measures. *Sbornik: Mathematics*, 196(3):309, 2005.
- [5] Michael C Brennan, Daniele Bigoni, Olivier Zahm, Alessio Spantini, and Youssef Marzouk. Greedy inference with structure-exploiting lazy maps. *arXiv preprint arXiv:1906.00031*, 2020.
- [6] Abdellah Chkifa, Albert Cohen, Ronald DeVore, and Christoph Schwab. Sparse adaptive taylor approximation algorithms for parametric and stochastic elliptic PDEs. *ESAIM: Mathematical Modelling and Numerical Analysis*, 47(1):253–280, 2013.
- [7] Abdellah Chkifa, Albert Cohen, and Christoph Schwab. Breaking the curse of dimensionality in sparse polynomial approximation of parametric PDEs. *Journal de Mathématiques Pures et Appliquées*, 103(2):400–428, 2015.

- [8] Albert Cohen, Ronald Devore, and Christoph Schwab. Analytic regularity and polynomial approximation of parametric and stochastic elliptic PDE's. *Analysis and Applications*, 9(01):11–47, 2011.
- [9] Laurent Dinh, Jascha Sohl-Dickstein, and Samy Bengio. Density estimation using Real NVP. *arXiv preprint arXiv:1605.08803*, 2016.
- [10] Alireza Doostan and Houman Owhadi. A non-adapted sparse approximation of PDEs with stochastic inputs. *Journal of Computational Physics*, 230(8):3015–3034, 2011.
- [11] Conor Durkan, Artur Bekasov, Iain Murray, and George Papamakarios. Neural spline flows. In *Advances in Neural Information Processing Systems*, pages 7509–7520, 2019.
- [12] Mathieu Germain, Karol Gregor, Iain Murray, and Hugo Larochelle. Made: Masked autoencoder for distribution estimation. In *International Conference on Machine Learning*, pages 881–889, 2015.
- [13] Gustaf Gripenberg. Unconditional bases of wavelets for Sobolev spaces. *SIAM Journal on Mathematical Analysis*, 24(4):1030–1042, 1993.
- [14] Chin-Wei Huang, David Krueger, Alexandre Lacoste, and Aaron Courville. Neural Autoregressive Flows. In *International Conference on Machine Learning*, pages 2083–2092, 2018.
- [15] Priyank Jaini, Kira A Selby, and Yaoliang Yu. Sum-of-Squares Polynomial Flow. In *International Conference on Machine Learning*, pages 3009–3018, 2019.
- [16] Durk P Kingma and Prafulla Dhariwal. Glow: Generative flow with invertible 1x1 convolutions. In *Advances in Neural Information Processing Systems*, pages 10215–10224, 2018.
- [17] Herbert Knothe. Contributions to the theory of convex bodies. *The Michigan Mathematical Journal*, 4:39–52, 1957.
- [18] Ivan Kobyzev, Simon Prince, and Marcus A Brubaker. Normalizing flows: Introduction and ideas. *arXiv preprint arXiv:1908.09257*, 2019.
- [19] Han Liu, John Lafferty, and Larry Wasserman. The nonparanormal: Semiparametric estimation of high dimensional undirected graphs. *Journal of Machine Learning Research*, 10(Oct):2295–2328, 2009.
- [20] Andrew J Majda and John Harlim. *Filtering complex turbulent systems*. Cambridge University Press, 2012.
- [21] Youssef Marzouk, Tarek Moselhy, Matthew Parno, and Alessio Spantini. *Sampling via Measure Transport: An Introduction*, pages 1–41. Springer International Publishing, 2016.
- [22] Rebecca Morrison, Ricardo Baptista, and Youssef Marzouk. Beyond normality: Learning sparse probabilistic graphical models in the non-Gaussian setting. In *Advances in Neural Information Processing Systems*, pages 2359–2369, 2017.
- [23] Benjamin Muckenhoupt. Hardy's inequality with weights. *Studia Mathematica*, 44(1):31–38, 1972.
- [24] Jorge Nocedal and Stephen Wright. *Numerical optimization*. Springer Science & Business Media, 2006.
- [25] Aaron van den Oord, Yazhe Li, Igor Babuschkin, Karen Simonyan, Oriol Vinyals, Koray Kavukcuoglu, George van den Driessche, Edward Lockhart, Luis C Cobo, Florian Stimberg, et al. Parallel WaveNet: Fast high-fidelity speech synthesis. *arXiv preprint arXiv:1711.10433*, 2017.
- [26] George Papamakarios and Iain Murray. Fast ε -free inference of simulation models with Bayesian conditional density estimation. In *Advances in Neural Information Processing Systems*, pages 1028–1036, 2016.

- [27] George Papamakarios, Eric Nalisnick, Danilo Jimenez Rezende, Shakir Mohamed, and Balaji Lakshminarayanan. Normalizing flows for probabilistic modeling and inference. *arXiv preprint arXiv:1912.02762*, 2019.
- [28] George Papamakarios, Theo Pavlakou, and Iain Murray. Masked autoregressive flow for density estimation. In *Advances in Neural Information Processing Systems*, pages 2338–2347, 2017.
- [29] Matthew D Parno and Youssef M Marzouk. Transport map accelerated Markov chain Monte Carlo. *SIAM/ASA Journal on Uncertainty Quantification*, 6(2):645–682, 2018.
- [30] Danilo Jimenez Rezende and Shakir Mohamed. Variational inference with normalizing flows. *arXiv preprint arXiv:1505.05770*, 2015.
- [31] Murray Rosenblatt. Remarks on a multivariate transformation. *The Annals of Mathematical Statistics*, 23(3):470–472, 1952.
- [32] Jonas Rothfuss, Fabio Ferreira, Simon Walther, and Maxim Ulrich. Conditional density estimation with neural networks: Best practices and benchmarks. *arXiv:1903.00954*, 2019.
- [33] Bernard W Silverman. On the estimation of a probability density function by the maximum penalized likelihood method. *The Annals of Statistics*, pages 795–810, 1982.
- [34] Alessio Spantini, Ricardo Baptista, and Youssef Marzouk. Coupling techniques for nonlinear ensemble filtering. *arXiv preprint arXiv:1907.00389*, 2019.
- [35] Alessio Spantini, Daniele Bigoni, and Youssef Marzouk. Inference via low-dimensional couplings. *The Journal of Machine Learning Research*, 19(1):2639–2709, 2018.
- [36] Esteban G Tabak and Cristina V Turner. A family of nonparametric density estimation algorithms. *Communications on Pure and Applied Mathematics*, 66(2):145–164, 2013.
- [37] Vladimir Temlyakov. *Greedy approximation*, volume 20. Cambridge University Press, 2011.
- [38] Brian L Trippe and Richard E Turner. Conditional density estimation with Bayesian normalising flows. In *Bayesian Deep Learning: NIPS 2017 Workshop*, 2018.
- [39] Cédric Villani. *Optimal transport: old and new*, volume 338. Springer Science & Business Media, 2008.
- [40] Larry Wasserman. *All of statistics: a concise course in statistical inference*. Springer Science & Business Media, 2013.
- [41] Antoine Wehenkel and Gilles Louppe. Unconstrained monotonic neural networks. In *Advances in Neural Information Processing Systems*, pages 1543–1553, 2019.
- [42] Li Wenliang, Dougal Sutherland, Heiko Strathmann, and Arthur Gretton. Learning deep kernels for exponential family densities. In *International Conference on Machine Learning*, pages 6737–6746, 2019.
- [43] Anja Wille, Philip Zimmermann, Eva Vranová, Andreas Fürholz, Oliver Laule, Stefan Bleuler, Lars Hennig, Amela Prelić, Peter von Rohr, Lothar Thiele, et al. Sparse graphical Gaussian modeling of the isoprenoid gene network in arabidopsis thaliana. *Genome biology*, 5(11):R92, 2004.

Supplementary Material

Here we collect the proofs, additional results and details pertaining to the experiments. §SM.1 provides the proofs for the theoretical results on the optimization problem that are presented in §3. §SM.2 provides the complete adaptive algorithm for learning each map component that is described in §4. §SM.3 presents additional numerical results to demonstrate the expressiveness of the selected map representation. Lastly, §SM.4-SM.5 provide the details for the numerical experiments and the hyperparameters of the density estimation methods that are compared to the ATM algorithm in §5.

SM.1 Properties of the optimization problem

In Lemma 1 below, we show that the constrained optimization problem for each map component is strictly convex. Then we prove Propositions 1 and 2.

Lemma 1. *The optimization problem $\min_{\{s: \partial_k s > 0\}} \mathcal{J}_k(s)$ is strictly convex.*

Proof. Let $S_1^k, S_2^k : \mathbb{R}^k \rightarrow \mathbb{R}$ be two strictly increasing functions with respect to x_k , i.e., $\partial_k S_1^k(\mathbf{x}_{1:k}) > 0$ and $\partial_k S_2^k(\mathbf{x}_{1:k}) > 0$. Let $S^k = tS_1^k + (1-t)S_2^k$ for $t \in [0, 1]$. Then we have $\partial_k S^k(\mathbf{x}_{1:k}) = t\partial_k S_1^k(\mathbf{x}_{1:k}) + (1-t)\partial_k S_2^k(\mathbf{x}_{1:k}) > 0$ and the set of strictly increasing functions in x_k is convex.

From the sum of two strictly convex functions $x \mapsto \frac{1}{2}x^2$ and $x \mapsto -\log(x)$, then $s \mapsto \frac{1}{2}s^2 - \log(\partial_k s)$ is strictly convex with respect to s . It follows that $s \mapsto \mathcal{J}_k(s)$ where $\mathcal{J}_k(s) = \mathbb{E}_\pi[\frac{1}{2}s(\mathbf{X}_{1:k})^2 - \log|\partial_k s(\mathbf{X}_{1:k})|]$ is also strictly convex.

Therefore, $\min_{\{s: \partial_k s > 0\}} \mathcal{L}_k(s)$ is strictly convex and, moreover, has a unique global minimum. \square

Next, we prove Proposition 1.

Proof of Proposition 1. Let ξ be such that $\nabla j \circ r(\xi) = \nabla r(\xi) \cdot \nabla j(r(\xi)) = 0$. Because $\nabla r(\xi) \in \mathbb{R}^{m \times m}$ is invertible, we obtain $\nabla j(r(\xi)) = 0$ so that $r(\xi)$ is a critical point of j . By convexity of j , $r(\xi)$ is a global minimum of j and so ξ is a global minimum of $j \circ r$. Moreover, if j is strictly convex, $r(\xi)$ is the unique global minimum of j and so ξ is the unique global minimum of $j \circ r$. \square

Now we prepare to prove the results in Proposition 2, regarding the boundedness and continuity of the function $\mathcal{L}_k : H^{1,k}(\mathbb{R}^k) \rightarrow \mathbb{R}$ introduced in §3. The Proposition assumes the following condition on the target density π

$$\pi(\mathbf{x}) \leq C_\pi \eta(\mathbf{x}). \quad (\text{SM.12})$$

Before stating the proof, we note several relevant properties of the modified soft-plus function g and then recall two results from functional analysis.

First, the function $g(\xi) = \log(1 + 2^\xi)/\log(2)$ satisfies the following properties for all $\xi, \xi' \in \mathbb{R}$:

$$|g(\xi)| \leq 1 + |\xi| \quad (\text{SM.13})$$

$$|\log(g(\xi))| \leq |\xi| \quad (\text{SM.14})$$

$$|g(\xi) - g(\xi')| \leq |\xi - \xi'| \quad (\text{SM.15})$$

$$|\log(g(\xi)) - \log(g(\xi'))| \leq |\xi - \xi'| \quad (\text{or even } \leq \log(2)|\xi - \xi'|). \quad (\text{SM.16})$$

Second, we recall the well-known Trace theorem [1].

Theorem 2. *For $f \in H^{1,k}(\mathbb{R}^k)$ we have*

$$\int_{\mathbb{R}^{k-1}} f(\mathbf{x}_{<k}, 0)^2 d\mathbf{x}_{<k} \leq \|f\|_{H^{1,k}}^2. \quad (\text{SM.17})$$

Proof of Theorem 2. For any $u \in H^1(\mathbb{R})$ we have

$$u(0)^2 = \int_{-\infty}^0 2u(\xi)u'(\xi)d\xi \leq \int_{-\infty}^0 |u(\xi)|^2 + |u'(\xi)|^2 d\xi \leq \int_{-\infty}^{+\infty} |u(\xi)|^2 + |u'(\xi)|^2 d\xi.$$

Setting $u(\xi) = f(\mathbf{x}_{<k}, \xi)$ and integrating both sides over $\mathbf{x}_{<k} \in \mathbb{R}^{k-1}$ gives the result. \square

Third, we recall a simplified form of the generalized integral Hardy inequality [23].

Theorem 3. *For weight $\rho : \mathbb{R}_+ \rightarrow \mathbb{R}_+$ and $u \in L_\rho^2(\mathbb{R})$, there exists a constant $C_h < \infty$ such that*

$$\int_0^{+\infty} \left(\int_0^x u(t)dt \right)^2 \rho(x)dx \leq C_h \int_0^{+\infty} u(x)^2 \rho(x)dx \quad (\text{SM.18})$$

if and only if

$$\sup_{x>0} \left(\int_x^{+\infty} \rho(t)dt \right)^{1/2} \left(\int_0^x \rho(t)^{-1}dt \right)^{1/2} < +\infty. \quad (\text{SM.19})$$

From the Hardy inequality in Theorem 3, we have the following result.

Lemma 4. *For the standard Gaussian density $\eta(\mathbf{x})$ and $v \in L^2_\eta(\mathbb{R}^k)$, then*

$$\int_{\mathbb{R}^k} \left(\int_0^{x_k} v(\mathbf{x}_{<k}, t) dt \right)^2 \eta(\mathbf{x}_{1:k}) d\mathbf{x}_{1:k} \leq C_h \int_{\mathbb{R}^k} v(\mathbf{x}_{1:k})^2 \eta(\mathbf{x}_{1:k}) d\mathbf{x}_{1:k}. \quad (\text{SM.20})$$

Proof of Lemma 4. For the one-dimensional standard Gaussian marginal $\rho(x_k) = \eta(x_k)$, we have

$$\left(\int_x^{+\infty} \rho(t) dt \right)^{1/2} \left(\int_0^x \rho(t)^{-1} dt \right)^{1/2} = \left(\int_x^{+\infty} e^{-t^2/2} dt \right)^{1/2} \left(\int_0^x e^{t^2/2} dt \right)^{1/2} := D(x).$$

$D(x)$ is a continuous function of x with a finite limit as $x \rightarrow 0$. Thus, it is sufficient to consider its asymptotic behavior to show it is bounded for all $x > 0$.

For $x > 1$, we have $\int_x^{+\infty} e^{-t^2/2} dt \leq e^{-x^2/2}$ and $D(x)^2 \leq e^{-x^2/2} \int_0^x e^{t^2/2} dt$, which is related to the well-known Dawson function. Using integration-by-parts we have $\int_0^x e^{t^2/2} dt = \int_0^1 e^{t^2/2} dt + e^{x^2/2}/x - \sqrt{e} + \int_1^x e^{t^2/2}/t^2 dt$. As $x \rightarrow \infty$ the dominating term in the sum is $e^{x^2/2}/x$. Thus, $e^{-x^2/2} \int_0^x e^{t^2/2} dt$ behaves asymptotically as $\mathcal{O}(\frac{1}{x})$, and the bounded condition in (SM.19) holds for the standard Gaussian density $\eta(x_k)$.

Thus, by the Hardy inequality in (SM.18) for $u \in L^2_\eta(\mathbb{R})$, we have

$$\int_0^{+\infty} \left(\int_0^{x_k} u(t) dt \right)^2 \eta(x_k) dx_k \leq C_h \int_0^{+\infty} u(x_k)^2 \eta(x_k) dx_k. \quad (\text{SM.21})$$

For the symmetric density $\eta(x_k) = \eta(-x_k)$ we also have

$$\int_{-\infty}^0 \left(\int_0^{x_k} u(t) dt \right)^2 \eta(x_k) dx_k \leq C_h \int_{-\infty}^0 u(x_k)^2 \eta(x_k) dx_k. \quad (\text{SM.22})$$

Combining the results in (SM.21) and (SM.22), we have

$$\int_{-\infty}^{+\infty} \left(\int_0^{x_k} u(t) dt \right)^2 \eta(x_k) dx_k \leq C_h \int_{-\infty}^{+\infty} u(x_k)^2 \eta(x_k) dx_k.$$

Setting $u(t) = v(\mathbf{x}_{<k}, t)$ and integrating both sides over $\mathbf{x}_{<k} \in \mathbb{R}^{k-1}$ with the standard Gaussian weight function $\eta(\mathbf{x}_{<k})$ gives the result. \square

Lastly, we note that η is a bounded density on \mathbb{R}^d . We denote its maximum value by

$$C_\eta := \max_{\mathbf{x} \in \mathbb{R}^d} \eta(\mathbf{x}) = (2\pi)^{-d/2}. \quad (\text{SM.23})$$

Proof of Proposition 2. To show that

$$\mathcal{L}_k(f) = \mathbb{E}_\pi \left[\frac{1}{2} \left(f(\mathbf{x}_{<k}, 0) + \int_0^{x_k} g(\partial_k f(\mathbf{x}_{<k}, t)) dt \right)^2 - \log g(\partial_k f(\mathbf{x}_{1:k})) \right]$$

is finite for any $f \in H^{1,k}(\mathbb{R}^k)$, it suffices to show that the three terms $\mathbb{E}_\pi[f(\mathbf{x}_{<k}, 0)^2]$, $\mathbb{E}_\pi[(\int_0^{x_k} g(\partial_k f(\mathbf{x}_{<k}, t)) dt)^2]$, and $\mathbb{E}_\pi[\log g(\partial_k f(\mathbf{x}_{1:k}))^2]$ are finite.

For the first term, by the bounds on π and η and the Trace theorem, we have

$$\begin{aligned} \mathbb{E}_\pi[f(\mathbf{x}_{<k}, 0)^2] &\stackrel{(\text{SM.12})}{\leq} C_\pi \int_{\mathbb{R}^k} f(\mathbf{x}_{<k}, 0)^2 \eta(\mathbf{x}_{1:k}) d\mathbf{x}_{1:k} \\ &= C_\pi \int_{\mathbb{R}^{k-1}} f(\mathbf{x}_{<k}, 0)^2 \eta(\mathbf{x}_{<k}) d\mathbf{x}_{<k} \\ &\stackrel{(\text{SM.17})}{\leq} C_\pi C_\eta \|f\|_{H^{1,k}}^2. \end{aligned}$$

For the second term, by the bounds on π and η , the upper bound for g , and the Hardy inequality, we have

$$\begin{aligned}
\mathbb{E}_\pi \left[\left(\int_0^{x_k} g(\partial_k f(\mathbf{x}_{<k}, t)) dt \right)^2 \right] &\stackrel{\text{(SM.12)}}{\leq} C_\pi \mathbb{E}_\eta \left[\left(\int_0^{x_k} g(\partial_k f(\mathbf{x}_{<k}, t)) dt \right)^2 \right] \\
&\stackrel{\text{(SM.20)}}{\leq} C_\pi C_h \mathbb{E}_\eta [g(\partial_k f(\mathbf{x}_{1:k}))^2] \\
&\stackrel{\text{(SM.13)}}{\leq} 2C_\pi C_h \mathbb{E}_\eta [1 + (\partial_k f(\mathbf{x}_{1:k}))^2] \\
&\stackrel{\text{(SM.23)}}{\leq} 2C_\pi C_h (1 + C_\eta \|f\|_{H^{1,k}}^2).
\end{aligned}$$

For the last term, using the properties of g , we have

$$\begin{aligned}
\mathbb{E}_\pi [\log g(\partial_k f(\mathbf{x}_{1:k}))^2] &\stackrel{\text{(SM.14)}}{\leq} \mathbb{E}_\pi [(\partial_k f(\mathbf{x}_{1:k}))^2] \\
&\stackrel{\text{(SM.12)}}{\leq} C_\pi \mathbb{E}_\eta [(\partial_k f(\mathbf{x}_{1:k}))^2] \\
&\leq C_\pi C_\eta \|f\|_{H^{1,k}}^2.
\end{aligned}$$

We now prove that the objective \mathcal{L}_k is a continuous function from $H^{1,k}(\mathbb{R}^k)$ to \mathbb{R} .

We first observe that the difference of the objective function evaluated at $f_1, f_2 \in H^{1,k}(\mathbb{R}^k)$ is bounded using the triangle inequality as

$$\begin{aligned}
|\mathcal{L}_k(f_1) - \mathcal{L}_k(f_2)| &= \left| \mathbb{E}_\pi \left[\frac{1}{2} \mathcal{R}(f_1)^2 - \frac{1}{2} \mathcal{R}(f_2)^2 - \log(\partial_k \mathcal{R}(f_1)) + \log(\partial_k \mathcal{R}(f_2)) \right] \right| \\
&\leq \frac{1}{2} \mathbb{E}_\pi |\mathcal{R}(f_1)^2 - \mathcal{R}(f_2)^2| + \mathbb{E}_\pi |\log(\partial_k \mathcal{R}(f_1)) - \log(\partial_k \mathcal{R}(f_2))|. \quad \text{(SM.24)}
\end{aligned}$$

For the first term in (SM.24), we have

$$\begin{aligned}
\frac{1}{2} \mathbb{E}_\pi |\mathcal{R}(f_1)^2 - \mathcal{R}(f_2)^2| &= \frac{1}{2} \mathbb{E}_\pi |(\mathcal{R}(f_1) - \mathcal{R}(f_2))(\mathcal{R}(f_1) + \mathcal{R}(f_2))| \\
&\leq \frac{1}{2} \left(\mathbb{E}_\pi |\mathcal{R}(f_1) - \mathcal{R}(f_2)|^2 \right)^{1/2} \left(\mathbb{E}_\pi |\mathcal{R}(f_1) + \mathcal{R}(f_2)|^2 \right)^{1/2}.
\end{aligned}$$

The terms $\mathbb{E}_\pi [\mathcal{R}(f_1)^2]$, $\mathbb{E}_\pi [\mathcal{R}(f_2)^2]$ and thus $\mathbb{E}_\pi [(\mathcal{R}(f_1) + \mathcal{R}(f_2))^2]$ are finite for $f_1, f_2 \in H^{1,k}(\mathbb{R}^k)$ by the result above. The term containing the squared difference of the operator \mathcal{R}_k applied to f_1 and f_2 is bounded by the sum of two terms as

$$\begin{aligned}
\mathbb{E}_\pi |\mathcal{R}_k(f_1) - \mathcal{R}_k(f_2)|^2 &= \int_{\mathbb{R}^k} \left(\mathcal{R}_k(f_1)(\mathbf{x}_{1:k}) - \mathcal{R}_k(f_2)(\mathbf{x}_{1:k}) \right)^2 \pi(\mathbf{x}_{1:k}) d\mathbf{x}_{1:k} \\
&\leq 2 \int_{\mathbb{R}^k} \left(f_1(\mathbf{x}_{<k}, 0) - f_2(\mathbf{x}_{<k}, 0) \right)^2 \pi(\mathbf{x}_{1:k}) d\mathbf{x}_{1:k} \\
&\quad + 2 \int_{\mathbb{R}^k} \left(\int_0^{x_k} g(\partial_k f_1(\mathbf{x}_{<k}, t)) - g(\partial_k f_2(\mathbf{x}_{<k}, t)) dt \right)^2 \pi(\mathbf{x}_{1:k}) d\mathbf{x}_{1:k}.
\end{aligned}$$

Using the bounds on π and η and the Trace theorem, we have

$$\begin{aligned}
&\int_{\mathbb{R}^k} \left(f_1(\mathbf{x}_{<k}, 0) - f_2(\mathbf{x}_{<k}, 0) \right)^2 \pi(\mathbf{x}_{1:k}) d\mathbf{x}_{1:k} \\
&\stackrel{\text{(SM.12)}}{\leq} C_\pi \int_{\mathbb{R}^k} \left(f_1(\mathbf{x}_{<k}, 0) - f_2(\mathbf{x}_{<k}, 0) \right)^2 \eta(\mathbf{x}_{1:k}) d\mathbf{x}_{1:k} \\
&= C_\pi \int_{\mathbb{R}^{k-1}} \left(f_1(\mathbf{x}_{<k}, 0) - f_2(\mathbf{x}_{<k}, 0) \right)^2 \eta(\mathbf{x}_{<k}) d\mathbf{x}_{<k} \\
&\stackrel{\text{(SM.17)}}{\leq} C_\pi C_\eta \|f_1 - f_2\|_{H^{1,k}}^2.
\end{aligned}$$

Applying the Hardy inequality and using the Lipschitz continuity of $g(\xi)$, we have

$$\begin{aligned}
& \int_{\mathbb{R}^k} \left(\int_0^{x_k} g(\partial_k f_1(\mathbf{x}_{<k}, t)) - g(\partial_k f_2(\mathbf{x}_{<k}, t)) dt \right)^2 \pi(\mathbf{x}_{1:k}) d\mathbf{x}_{1:k} \\
& \stackrel{(\text{SM.12})}{\leq} C_\pi \int_{\mathbb{R}^k} \left(\int_0^{x_k} g(\partial_k f_1(\mathbf{x}_{<k}, t)) - g(\partial_k f_2(\mathbf{x}_{<k}, t)) dt \right)^2 \eta(\mathbf{x}_{1:k}) d\mathbf{x}_{1:k} \\
& \stackrel{(\text{SM.20})}{\leq} C_\pi C_h \int_{\mathbb{R}^k} \left(g(\partial_k f_1(\mathbf{x}_{1:k})) - g(\partial_k f_2(\mathbf{x}_{1:k})) \right)^2 \eta(\mathbf{x}_{1:k}) d\mathbf{x}_{1:k} \\
& \stackrel{(\text{SM.23})}{\leq} C_\pi C_h C_\eta \int_{\mathbb{R}^k} \left(g(\partial_k f_1(\mathbf{x}_{1:k})) - g(\partial_k f_2(\mathbf{x}_{1:k})) \right)^2 d\mathbf{x}_{1:k} \\
& \stackrel{(\text{SM.15})}{\leq} C_\pi C_h C_\eta \int_{\mathbb{R}^k} \left(\partial_k f_1(\mathbf{x}_{1:k}) - \partial_k f_2(\mathbf{x}_{1:k}) \right)^2 d\mathbf{x}_{1:k} \\
& \leq C_\pi C_h C_\eta \|f_1 - f_2\|_{H^{1,k}}^2.
\end{aligned}$$

Thus, for $\|f_1 - f_2\|_{H^{1,k}} \rightarrow 0$ we have $\mathbb{E}_\pi |\mathcal{R}(f_1) - \mathcal{R}(f_2)|^2 \rightarrow 0$ and $\mathbb{E}_\pi |\mathcal{R}(f_1)^2 - \mathcal{R}(f_2)^2| \rightarrow 0$.

For the second term in (SM.24), by the Lipschitz continuity of $\log(g(\xi))$, we have

$$\begin{aligned}
\mathbb{E}_\pi |\log(\partial_k \mathcal{R}(f_1)) - \log(\partial_k \mathcal{R}(f_2))| &= \mathbb{E}_\pi |\log(g(\partial_k f_1)) - \log(g(\partial_k f_2))| \\
&\stackrel{(\text{SM.16})}{\leq} \mathbb{E}_\pi |\partial_k f_1(\mathbf{x}_{1:k}) - \partial_k f_2(\mathbf{x}_{1:k})| \\
&\leq \left(\mathbb{E}_\pi |\partial_k f_1(\mathbf{x}_{1:k}) - \partial_k f_2(\mathbf{x}_{1:k})|^2 \right)^{1/2} \\
&\stackrel{(\text{SM.12})}{\leq} \left(C_\pi \mathbb{E}_\eta |\partial_k f_1(\mathbf{x}_{1:k}) - \partial_k f_2(\mathbf{x}_{1:k})|^2 \right)^{1/2} \\
&\stackrel{(\text{SM.23})}{\leq} \sqrt{C_\pi C_\eta} \|f_1 - f_2\|_{H^{1,k}}
\end{aligned}$$

Combining the results for the convergence of both terms in (SM.24), for $f_1 \rightarrow f_2$ in $H^{1,k}(\mathbb{R}^k)$ we have $\mathcal{L}_k(f_1) \rightarrow \mathcal{L}_k(f_2)$ in \mathbb{R} . \square

SM.2 Adaptive transport map algorithm

In this section, we include the complete procedure for the Adaptive Transport Map (ATM) algorithm presented in §4 of the main text.

Algorithm 1 Estimate k -th map component S^k

- 1: **Input:** n training samples $\{\mathbf{x}_{1:k}^i\}_{i=1}^n$, number of features m
 - 2: Initialize $\Lambda_0 = \emptyset$, $f_0 = 0$
 - 3: **for** $t = 1, \dots, m$ **do**
 - 4: Find reduced margin: Λ_t^{RM}
 - 5: Select new feature's multi-index: $\alpha_t^* \in \arg \max_{\alpha \in \Lambda_t^{\text{RM}}} |\nabla_{c_\alpha} \hat{\mathcal{L}}_k(f_{t-1})|$
 - 6: Update active set: $\Lambda_t = \Lambda_{t-1} \cup \alpha_t^*$
 - 7: Update approximation: $f_t = \arg \min_{f \in \text{span}(\psi_{\Lambda_t})} \hat{\mathcal{L}}_k(f)$
 - 8: **end for**
 - 9: **Output:** $\hat{S}^k = \mathcal{R}_k(f_t)$
-

SM.3 Additional numerical experiments

To demonstrate the expressiveness of the Hermite functions for approximating the components of the Knothe–Rosenblatt rearrangement, we tested the ATM algorithm on a suite of two dimensional distributions with various geometries. These include the Banana, Funnel, Cosine, Mixture of Gaussians (MoG), and Ring densities π that were considered in [42, 15]. For each density, we

generate $n = 10^4$ i.i.d. samples from π and apply a random rotation to the data using a uniformly distributed angle in $[0, \pi/2]$. Figure SM.6 plots the true densities π and the approximate densities $\hat{\pi} := \hat{S}^\# \eta$ found using ATM with up to $m = 250$ features.

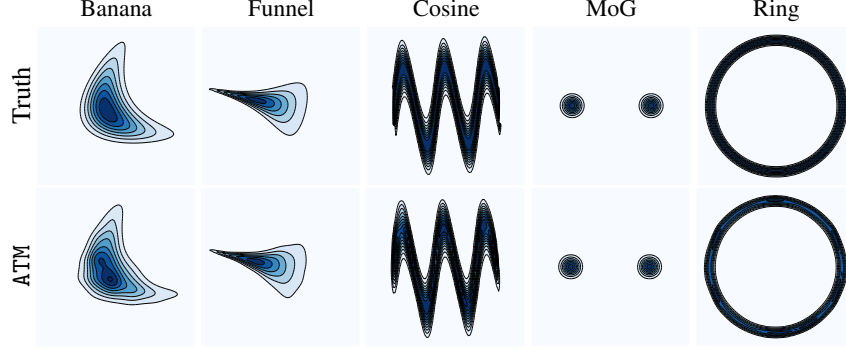


Figure SM.6: The densities π and $\hat{\pi}$ for 5 datasets using $n = 10^4$ samples

SM.4 Details for numerical experiments

In this section, we include additional details on the setup of the gene and UCI datasets in §SM.4.1 and the Lorenz-96 dataset in §SM.4.2.

For all datasets, we apply a linear transformation to each sample in the training and test sets by subtracting the empirical mean of the training samples and dividing by the empirical standard deviation of the training samples. The negative log-likelihoods of the approximate densities from all algorithms are evaluated on the standardized test sets. We subtract the log of the empirical standard deviation from the negative log-likelihood to assess the density approximations for the *original* random variables, prior to the linear transformation.

SM.4.1 Gene and UCI datasets

For the gene dataset, we follow the procedure in [19] and apply a log transformation to each gene expression level before estimating the density.

To define multiple datasets for each example, we split the data into equal-sized and independent test sets. We consider 20 and 10 test sets for the gene and the UCI datasets, respectively. For each test set, we use the remaining samples as a training set to learn the transport map with the ATM algorithm and evaluate the negative log-likelihood of the approximate density at the samples in the test set. The mean negative log-likelihood over the sets of training samples is reported in Tables 1 and 3.

SM.4.2 Lorenz-96 dataset

The Lorenz-96 model describes the state of the atmosphere over time on one of the Earth's latitude circles. To define the system dynamics, we spatially discretize the state using d evenly spaced variables on a periodic lattice. The evolution of each state variable X_j is given by the set of coupled nonlinear ODEs

$$\frac{dX_j}{dt} = (X_{j+1} - X_{j-2})X_{j-1} - X_j + F, \quad j = 1, \dots, d, \quad (\text{SM.25})$$

with periodic boundary conditions $X_{-1} \equiv X_{d-1}$, $X_0 \equiv X_d$, and $X_1 \equiv X_{d+1}$. In our experiments we set the constant forcing parameter to $F = 8$, which leads to fully chaotic behavior [20].

To generate i.i.d. samples from the system's invariant (long-time) distribution, we sample n initial conditions from a multivariate standard Gaussian distribution. For each sample, we run the ODE in equation (SM.25) for $T = 40,000$ steps using the Runge-Kutta method with a time-step of $\Delta t = 0.01$. The samples of the state at the final time are then i.i.d. samples from the push-forward distribution of the standard Gaussian through the nonlinear forward dynamics for T steps.

SM.5 Architectures of other density estimation methods

In this subsection we present the details of the alternative (joint and conditional) density estimation methods to ATM that we consider in §5.

For the normalizing flow architectures in §5.2-5.3, we use the implementation of [28] for MAF and MADE and the implementation of [14] for NAF. The hyper-parameters we consider for MAF and MADE are: $\{1, 2\}$ hidden layers, $\{32, 64, 128, 256, 512\}$ hidden units in each layer, $\{5, 10\}$ flow layers, ReLu activation functions, and 10 mixture components for MADE-MoG and MAF-MADE. The hyper-parameters we consider for NAF are: deep dense sigmoidal flows with 1 hidden layer and 16 sigmoid units, 1 hidden layer for the parameter networks with $\{32, 64, 128, 256, 512\}$ hidden units in each layer, and 5 flow layers.

For each normalizing flow architecture we use the recommended stochastic gradient descent optimizer with a learning rate of 10^{-3} . We partition 10% of the samples in each dataset to be validation samples and use the remaining samples for training. We select the optimal hyper-parameters for each dataset by fitting the approximate density with the training data and selecting the parameters that minimize the negative log-likelihood of the approximate density on the validation samples. We also use the validation samples to set the termination criteria during the optimization.

For the conditional density estimation examples in §5.4-5.5, we follow the implementation of [32]. The hyper-parameters we consider for the neural networks in the MDN and NF models are: 2 hidden layers, 32 hidden units in each layer, $\{5, 10, 20, 50, 100\}$ centers or flows, weight normalization, and a dropout probability of 0.2 for regularizing the neural networks during training. For CKDE and NKDE we select the bandwidth of the kernel estimators using 5-fold cross-validation.